J Therm Spray Tech (2017) 26:1011–1024
DOI 10.1007/s11666-017-0574-1

PEER REVIEWED

$Yb_2Si_2O_7$ Environmental Barrier Coatings Deposited by Various Thermal Spray Techniques: A Preliminary Comparative Study

Emine Bakan[1] · Diana Marcano[1] · Dapeng Zhou[1] · Yoo Jung Sohn[1] · Georg Mauer[1] · Robert Vaßen[1]

Submitted: 5 December 2016 / in revised form: 2 May 2017 / Published online: 5 June 2017

Abstract Dense, crack-free, uniform, and well-adhered environmental barrier coatings (EBCs) are required to enhance the environmental durability of silicon (Si)-based ceramic matrix composites in high pressure, high gas velocity combustion atmospheres. This paper represents an assessment of different thermal spray techniques for the deposition of $Yb_2Si_2O_7$ EBCs. The $Yb_2Si_2O_7$ coatings were deposited by means of atmospheric plasma spraying (APS), high-velocity oxygen fuel spraying (HVOF), suspension plasma spraying (SPS), and very low-pressure plasma spraying (VLPPS) techniques. The initial feedstock, as well as the deposited coatings, were characterized and compared in terms of their phase composition. The as-sprayed amorphous content, microstructure, and porosity of the coatings were further analyzed. Based on this preliminary investigation, the HVOF process stood out from the other techniques as it enabled the production of vertical crack-free coatings with higher crystallinity in comparison with the APS and SPS techniques in atmospheric conditions. Nevertheless, VLPPS was found to be the preferred process for the deposition of $Yb_2Si_2O_7$ coatings with desired characteristics in a controlled-atmosphere chamber.

Keywords ceramic matrix composite (CMC) · environmental barrier coating (EBC) · thermal spray · ytterbium silicate

✉ Emine Bakan
e.bakan@fz-juelich.de

[1] Forschungszentrum Jülich GmbH, Institute of Energy and Climate Research IEK-1, 52425 Jülich, Germany

Introduction

An improvement in the temperature capability of high-strength materials is crucial for developments in advanced gas turbine technology. As current film-cooled and thermal barrier coating protected single-crystal superalloy components have already reached their limit in terms of performance, ceramic matrix composites (CMCs) are regarded as the new material of choice for such components. SiC/SiC CMCs, for example, offer higher temperature capability (about 400 °C higher compared to the best superalloy), good mechanical strength, thermal shock resistance, and, moreover, they are lightweight. These characteristics can be used to reduce the weight of aircraft, while higher turbine inlet temperatures are reached with less cooling air, which in turn result in greater efficiency.

One main obstacle to substituting Si-based ceramics for metallic components is their degradation when exposed to water vapor-rich fast-flowing gasses in high-temperature and pressure combustion environments (Ref 1-5). Furthermore, the CMCs suffer from severe hot corrosion in molten salt (Ref 6). Environmental barrier coatings (EBCs) (Ref 7) are therefore needed for the protection of Si-based CMCs in order to increase their durability in combustion environments. Beginning in the late 1990s, research and development at NASA introduced multilayer EBC systems, which were subsequently successfully tested in gas turbine engines (Ref 7-9). In these EBC systems, silicon bond coats were applied for the oxidation protection of the substrate as well as to improve the adhesion of the coatings on it. Different top coat layers with high water vapor stability were deposited on the silicon bond coats to impede the diffusion of oxygen and water vapor through the substrate. Mullite and barium-strontium-aluminosilicate (BSAS) were used for this purpose in the early generation EBCs (Ref 10). Lee et al. (Ref 11) later on experimentally

compared the environmental stability of BSAS and two types of RE silicates: mono- and disilicates (RE_2O_3-SiO_2 and RE_2O_3-$2SiO_2$) in combustion environments and observed that the RE monosilicates have a higher stability in water vapor than BSAS and RE disilicates. Furthermore, the superior chemical stability of some RE silicates (Yb, Lu, Sc silicates) compared to the BSAS was reported in this study and, consequently, later generation EBCs consisting of RE silicate top coats were established. In the meantime, the deposition of mullite and RE silicates by APS was investigated and found to be quite challenging due to the high glass-forming tendency of silicates and the high solidification rates in the process; as-sprayed coatings were reported to be highly amorphous (Ref 12). These issues are also familiar from the plasma spraying of YAG and hexaaluminate coatings (Ref 13-15). The amorphous deposits are not desired as crystallization induced shrinkage at elevated temperatures leads to crack formation and spallation of the coatings. To avoid that, NASA suggested a modification in the plasma spray process in which particles are sprayed on a substrate placed in a furnace and heated up to 1000 °C (Ref 16). Increasing the substrate temperature above the glass transformation temperature of the sprayed material ensures the nucleation and growth of the crystal nuclei, which results in highly crystalline silicate coatings being produced by this method (Ref 11, 17-19). Over the last two decades, EBC systems (e.g., bilayer, trilayer, multilayer) featuring different RE silicates were also manufactured using alternative processing techniques by different groups (Table 1). However, the same amorphous deposit problem was addressed for each deposition method in which the melting\-vaporization of the coating material and the subsequent rapid solidification of it on the substrate take place. When using wet chemical deposition methods, however, highly crystalline coatings were deposited. Nonetheless, a gaseous bubble formation was observed at the coating-substrate interface using the dip-coating technique, which likely has an adverse effect on the adhesion of the coatings. A sol-gel method involving high-temperature (1550 °C) sintering for densification of the layer does not seem to be applicable to a system that includes a Si bond layer, as it would exceed the melting temperature of Si (1400 °C). Ultimately, modified plasma spraying seems to be the only well-functioning technique among the other reported studies. However, the feasibility of transferring such spraying technology to real components with complicated shapes remains an important question.

Another processing issue of silicate EBCs is the deposition of stoichiometric coatings that are dense at the same time (Ref 26). Associated with the preferential volatilization of Si-bearing species from the molten particles during the spraying process, Si-depleted coatings were obtained when compared to starting powders. In particular, high-power processing to ensure dense silicate coatings was found to be conducive to the formation of stoichiometric coatings, since higher heat transfer from plasma to particles further boosts the evaporation of species with high vapor pressure (Ref 27). Similar processing issues and the resulting detrimental effects of secondary phases present in the as-sprayed coatings of different groups of materials (e.g., pyrochlores, perovskites) are often reported in the literature (Ref 28-31).

From a materials' perspective, Yb_2SiO_5 (YbMS) and $Yb_2Si_2O_7$ (YbDS) are the most extensively studied group of EBCs to date, as shown in Table 1. Although the investigation of Lee et al. (Ref 11) favors the potential of RE monosilicates with high stability against water, the comparison of YbMS and YbDS reveals a substantially higher coefficient of thermal expansion (CTE) of the former ($7.4 \times 10^{-6}\ K^{-1}$ (Ref 17)) than that of the latter ($4.1 \times 10^{-6}\ K^{-1}$ (Ref 26)) as well as of SiC ($4.7 \times 10^{-6}\ K^{-1}$). The significant CTE mismatch between YbMS and SiC is therefore said to result in the formation of unfavorable cracks, which provide diffusion paths to the oxygen and water vapor through the YbMS coatings (Ref 26).

Taking these findings into account, the YbDS coatings deposited by various thermal spray deposition

Table 1 EBC systems manufactured by means of different processing techniques

EBC system and materials	Process	References
Si/Mullite/YbMS or YbDS Si/YbDS	Plasma spray into a box furnace	Ref 11, 17-19, 20
LuDS/LuDS-Mullite/LuDS	Plasma spray	Ref 21
Mullite/GdMS	Slurry-based dip-coat processing	Ref 22
HfO_2-Si/(Yb,Gd)DS	Electron beam-physical vapor deposition (EB-PVD)	Ref 23
YMS	RF magnetron sputtering	Ref 24
LuDS	Sol-gel	Ref 25

MS and DS in the material compositions stand for mono- and disilicate, respectively

Table 2 Particle size of the $Yb_2Si_2O_7$ feedstock used for each individual thermal spray process

Thermal spray process	Particle size, μm		
	d_{10}	d_{50}	d_{90}
APS	24	38	68
HVOF	22	33	48
VLPPS	35	49	68
SPS	0.5	0.7	1.06

techniques were investigated in this study. The paper provides a comparison of the microstructure, crystallinity, and phase composition of YbDS coatings deposited by means of APS, high-velocity oxygen fuel (HVOF), suspension plasma spray (SPS), and very low-pressure plasma spraying (VLPPS).

Experimental

Powder Feedstock and Suspension

$Yb_2Si_2O_7$ powder provided by Oerlikon Metco (US) Inc. (Westbury, New York, USA) was used in this study for the deposition of coatings by APS. Part of this powder was sieved, and the particle fractions captured on and under the sieve were used for the VLPPS and HVOF processes, respectively. Particle size distributions of the fractions measured by laser diffraction (LA-950-V2, Horiba Ltd., Japan) and dynamic light scattering (LB-550, Horiba Ltd., Japan) are shown in Table 2. For the SPS process, the $Yb_2Si_2O_7$ powder was synthesized from stoichiometric amounts of YbO_2 (99.9%, Treibacher Industrie AG, Austria) and SiO_2 (99.5%, VWR International GmbH, Germany). An ethanol-based suspension of this mixture was mechanically activated in a tumbling mixer (150 min^{-1}) with ZrO_2 milling balls for 24 h. The obtained powder was dried and sintered at 1400 °C for 12 h. For SPS purposes, this powder was dispersed in ethanol with the addition of polyethylenimine (PEI) (Polysciences, Inc., Warrington, PA, USA) and ZrO_2 milling balls ($d = 3$ mm, Sigmund Lindner GmbH, Warmensteinach, Germany). The mixture was milled on a roller bank (120 min^{-1}, 24 h). The particle size values after milling are given in Table 2. Finally, the obtained suspension was diluted with ethanol to a final solid content of 10 wt.%. The dynamic viscosity of the suspension was determined by the Physica MCR 301 rheometer from Anton Paar, with the viscosity measured to be 1.55 mPa·s at a shear rate of 10 s^{-1}. Samples of each raw material were investigated by means of scanning electronic microscopy (SEM) (Carl Zeiss NTS GmbH, Oberkochen, Germany) and x-ray diffraction (XRD) (D4 Endeavor,

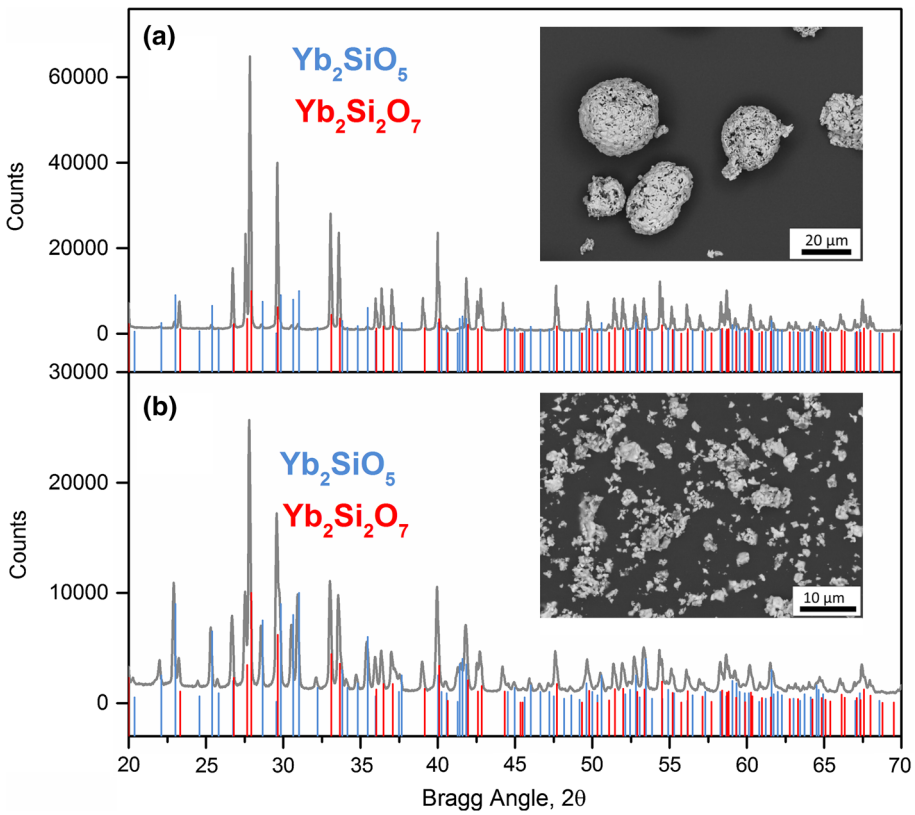

Fig. 1 XRD pattern of (a) micron- and (b) submicron-sized $Yb_2Si_2O_7$ powder (insets show the back-scattered SEM images of corresponding powders)

Bruker AXS GmbH, Karlsruhe, Germany) (Cu Kα radiation, operating voltage 40 kV, current 40 mA, step size 0.02°, step time 0.75 s, 2θ range of 10°-80°) for morphology and phase composition determination, respectively. XRD patterns of the micron-sized $Yb_2Si_2O_7$ powder (original powder, before sieving) with spherical particle morphology and submicron-sized $Yb_2Si_2O_7$ powder synthesized for the SPS process are shown in Fig. 1(a) and (b). Both XRD patterns yielded a crystalline structure with the presence of monoclinic $Yb_2Si_2O_7$ (*C2/m*, JCPDS No 01-082-0734) and secondary monoclinic Yb_2SiO_5 (*I2/a*, JCPDS No 00-040-0386) phases. Quantitative phase analysis (QPA) of the x-ray powder diffraction data was performed using the Rietveld analysis method (TOPAS software, Bruker Corporation, Germany), and micron- and submicron-sized powders were found to contain 5% and 39% Yb_2SiO_5, respectively.

Deposition of the Coatings

Four different thermal spray systems were operated for the deposition of $Yb_2Si_2O_7$ coatings. A MultiCoat system (Oerlikon Metco, Wohlen, Switzerland) with three-cathode TriplexPro 210 and Diamond Jet 2700 spray torches mounted on a six-axis robot (IRB 2400, ABB, Switzerland) was employed for APS and HVOF spray experiments, respectively. The HVOF burner was fitted with a convergent-cylindrical design nozzle (Type 2705) which yields lower particle velocities and thus longer dwell times in comparison with that of convergent-divergent nozzles (Ref 32). A VLPPS investigation was performed with an O3CP torch operated by the MultiCoat platform (Oerlikon Metco, Wohlen, Switzerland) in a controlled-atmosphere chamber. Finally, an Axial III plasma torch with three separate cathode-anode pairs (Mettech Northwestern Corp., North Vancouver, BC, Canada) was used to generate the plasma jet for the SPS study and feedstock material was injected into the center of this plasma plume. A suspension-feeding system developed by Forschungszentrum Jülich GmbH (Germany) was used for spraying (Ref 33). The spray parameters used for each experiment are listed in Table 3. High-power process conditions were selected for each spray method excluding the VLPPS technique to avoid vaporization but to obtain molten particles. Further information about the VLPPS method can be found here (Ref 34). The temperature of the samples was monitored with a 4 M8 pyrometer ($\lambda = 13$ μm) (Land Instruments GmbH, Leverkusen, Germany) in the APS, HVOF, and SPS processes and an IR-AP pyrometer ($\lambda = 1.6$ μm) (Chino Corporation, Tokyo, Japan) in the VLPPS process. Square shape graphite (20 × 20 × 15 mm) and carbon steel (25 × 25 × 2 mm) served as substrate materials. All substrates were grit-blasted to an arithmetic average roughness (R_a) value range of 4.0-5.5 μm and subsequently cleaned before spraying.

Table 3 Thermal spraying conditions for $Yb_2Si_2O_7$: APS, HVOF, VLPPS, and SPS

Parameters	Settings
APS	
Plasma gas composition, slpm	$46Ar/4H_2$
Current, A	520
Power, kW	57
Stand-off distance, mm	90
Robot speed, mm/s	500
Feed rate, %	30
Carrier gas, %	2.5
Number of passes	2
Cooling	None
Substrate temperature, °C	400
Deposition temperature, °C	575
HVOF	
Oxygen flow, slpm	395
Methane flow, slpm	190
Air flow, slpm	250
Feed rate, %	20
Stand-off distance, mm	325
Robot velocity, mm/s	1200
Number of passes	5
Cooling	None
Deposition temperature, °C	125-150
VLPPS	
Plasma gas composition, slpm	110Ar/20He
Chamber pressure, Pa	200
Feed rate, %	25
Current, A	2100
Stand-off distance, mm	700
Power, kW	90
Robot velocity, mm/s	15
Deposition temperature, °C	980
Deposition duration, min	2
SPS	
Plasma gas comp., slpm	$184Ar/37H_2/24.5N_2$
Current, A	250
Stand-off distance, mm	70
Feed rate, g/min	30
Robot velocity, mm/s	500
Number of passes	18
Deposition temperature, °C	500
Cooling	0.3 MPa press. air

The number of passes or deposition time for each set of parameters was adjusted to obtain 150-200 μm coating thickness

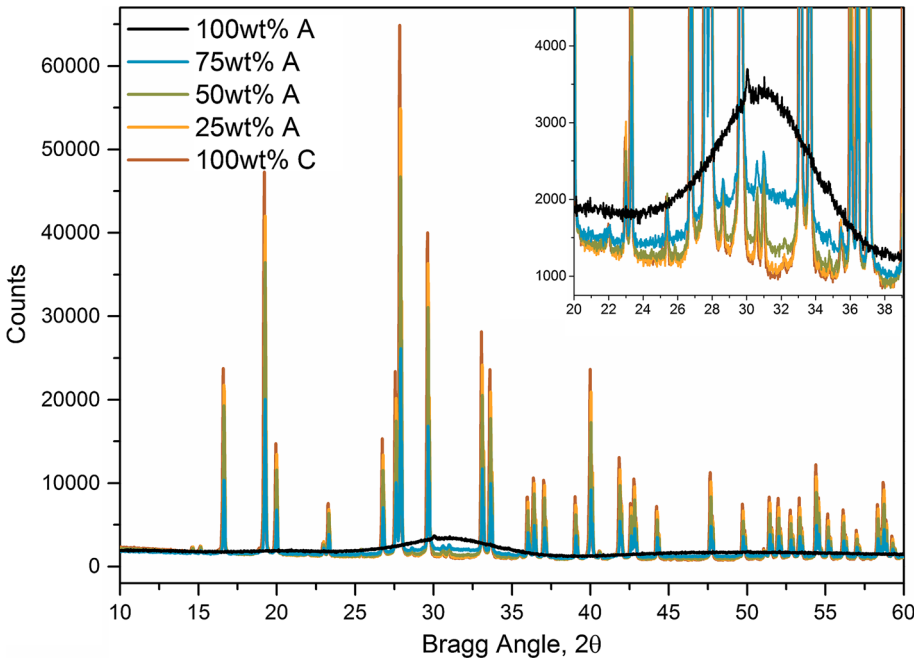

Fig. 2 XRD patterns of 100 wt.% A (A=amorphous), 75 wt.% A-25 wt.% C (C=crystalline), 50 wt.% A-50 wt.% C, 25 wt.% A-75 wt.% C, and 100 wt.% C powder and powder mixtures

Characterization of Deposited Coatings

Amorphous Content and Quantitative Phase Analysis (QPA)

XRD measurements were taken on the as-deposited top coats with the same measurement parameters for the feedstock given above (D4 Endeavor & TOPAS software, Bruker AXS, Germany). The presence of amorphous content in the XRD patterns of as-sprayed coatings was detected and since QPA using the Rietveld method is limited to well-defined crystalline species, the PONKCS (partial or no known crystal structure) method was used for this purpose. The advantages of the PONKCS method for the QPA of the amorphous phases over the traditional Rietveld method or Reference Intensity Ratio (RIR) analysis are reported here (Ref 35). In the Rietveld method, the weight fraction of the *i*th crystalline phase in a mixture of *n* phases can be obtained from

$$W_i = \frac{S_i(ZMV)_i}{\sum_{j=1}^{n} S_j(ZMV)_j} \quad \text{(Eq 1)}$$

where S_i is the Rietveld scale factor for phase *i*, *ZM* is the mass of the unit cell contents, and *V* is the volume of the unit cell. The PONKCS method also follows this general form, but it includes the empirically derived $(ZMV)_a$ of the amorphous (a) phase in Eq 1. $(ZMV)_a$ can be determined by using a known mixture of the amorphous and crystalline (c) sample for which the ZMV_c is known:

$$(ZMV)_a = \frac{W_a}{W_c}\frac{S_c}{S_a}(ZMV)_c \quad \text{(Eq 2)}$$

where W_a and W_c are the known weight fractions, S_a and S_c are the refined scale factors of the amorphous and crystalline samples, respectively. The background of the methodology is described in detail by Scarlett et al. (Ref 35). For the derivation of the $(ZMV)_a$, micron-sized $Yb_2Si_2O_7$ feedstock was used as the crystalline sample and the amorphous sample was obtained by plasma spraying the same powder into distilled cold water. Subsequently, amorphous-crystalline mixtures with weight fractions of 25-75, 50-50, 75-25 wt.% were prepared and analyzed by XRD as shown in Fig. 2. XRD patterns of 100 wt.% crystalline and 100 wt.% amorphous samples are also shown in Fig. 2 for comparison. Although a small peak at $\sim 30°$ of the 100 wt.% amorphous powder pattern was observed (see Fig. 2, inset graph), the powder was still assumed to be 100% amorphous for the analysis.

Microstructure and Porosity

The samples were sectioned, polished, and examined with a scanning electron microscope (Carl Zeiss NTS GmbH, Oberkochen, Germany) combined with an energy-dispersive x-ray INCAEnergy355 spectrometer (EDS, Oxford Instruments Ltd., Abingdon, Oxfordshire, UK). Acquired SEM images were employed to assess the volume fractions of pores in the coatings by means of image analysis using an image thresholding procedure with the analySIS pro software (Olympus Soft Imaging Solutions GmbH, Germany). The analysis was performed on 10 SEM micrographs (2000× magnification) per sample, each with a

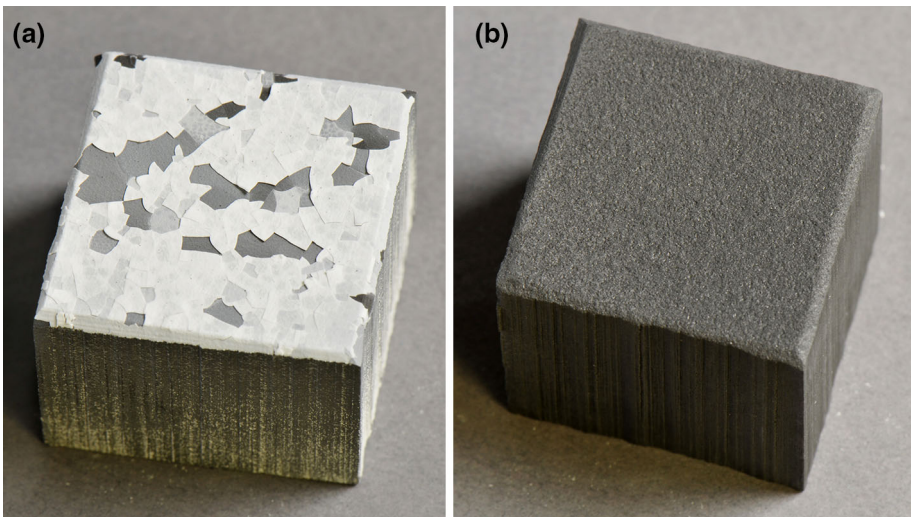

Fig. 3 First trials of $Yb_2Si_2O_7$ depositions by (a) SPS and (b) HVOF processes on graphite substrates

resolution of 1280 × 1100 pixels and covering a horizontal field width of 126 μm.

Results and Discussion

Coating Deposition

Graphite was used as the substrate material to deposit $Yb_2Si_2O_7$ coatings by different thermal spray techniques. The reason for testing with graphite in the first place was its relatively wide CTE (2–8 × 10^{-6} K^{-1} (Ref 36)) mean value range measured from polycrystalline graphite due to its anisotropy) to match with that of $Yb_2Si_2O_7$ (4.1 × 10^{-6} K^{-1} (Ref 26)). However, although APS- and VLPPS-deposited coatings remained adherent to graphite during and after deposition, suspension plasma sprayed coating flaked off during the cooling process and no coating could be deposited on graphite by HVOF Fig. 3. Although it remains unclear, the poor deposition by means of SPS on the graphite might be related to the sub-micron-sized feedstock, which contains 39% Yb_2SiO_5 (CTE, 7.4 × 10^{-6} K^{-1} (Ref 17)). As a result, possible higher thermal mismatch stresses arising upon cooling may be responsible for the spallation of the coating. No deposition acquired by HVOF, meanwhile, can be associated with the low mechanical strength of the graphite. It conceivably facilitates the removal of the graphite due to the impact of high-velocity particles and results in a "grit blasting" effect on the substrate instead of deposition. It was possible to obtain successful depositions by SPS and HVOF when the graphite substrates were substituted with carbon steel substrates.

Amorphous Content

The XRD patterns of the as-deposited $Yb_2Si_2O_7$ coatings using different thermal spray methods are shown in Fig. 4. Several reflection peaks and two broad humps (2θ range of 25°-38° and 40°-70°) that are observed in the patterns of the APS and SPS coatings clearly reveal an almost fully amorphous phase. Similarly, humps in the 2θ range of 25°-38° are also detectable in the patterns of the HVOF and VLPPS coatings, albeit relatively small and also accompanied with sharp, high-intensity peaks, which suggest the presence of crystalline phases.

$Yb_2Si_2O_7$ shows a type C disilicate structure according to the Felsche classification of RE silicates, and its SiO_4 tetrahedra units are known as glass formers (Ref 37, 38), as they produce highly viscous liquids when they melt. Although a solid crystalline phase is thermodynamically favorable for such liquid when it reaches its melting point, crystallization is kinetically restrained by its high viscosity. If this liquid is rapidly quenched as happens in the plasma spraying process, since the slow mobility of the molecules is further reduced to the point where they cannot move around and create new interfaces for nucleation, it solidifies as a glass. In order to enable crystal growth in this liquid, it would be ideal to allow nucleation above glass transition temperature (T_g) and to maintain this temperature, as crystal growth is a thermally activated process. To that end, aiming crystalline coatings, the practicality of reaching substrate temperatures as high as 1000 °C ($\sim T_g$) was investigated in each above-mentioned thermal spray process. To that end, the substrates were heated by spray torches prior to spraying. In APS and SPS, although it was initially possible to reach substrate temperatures of up to 800-900 °C (according to pyrometer recordings), the

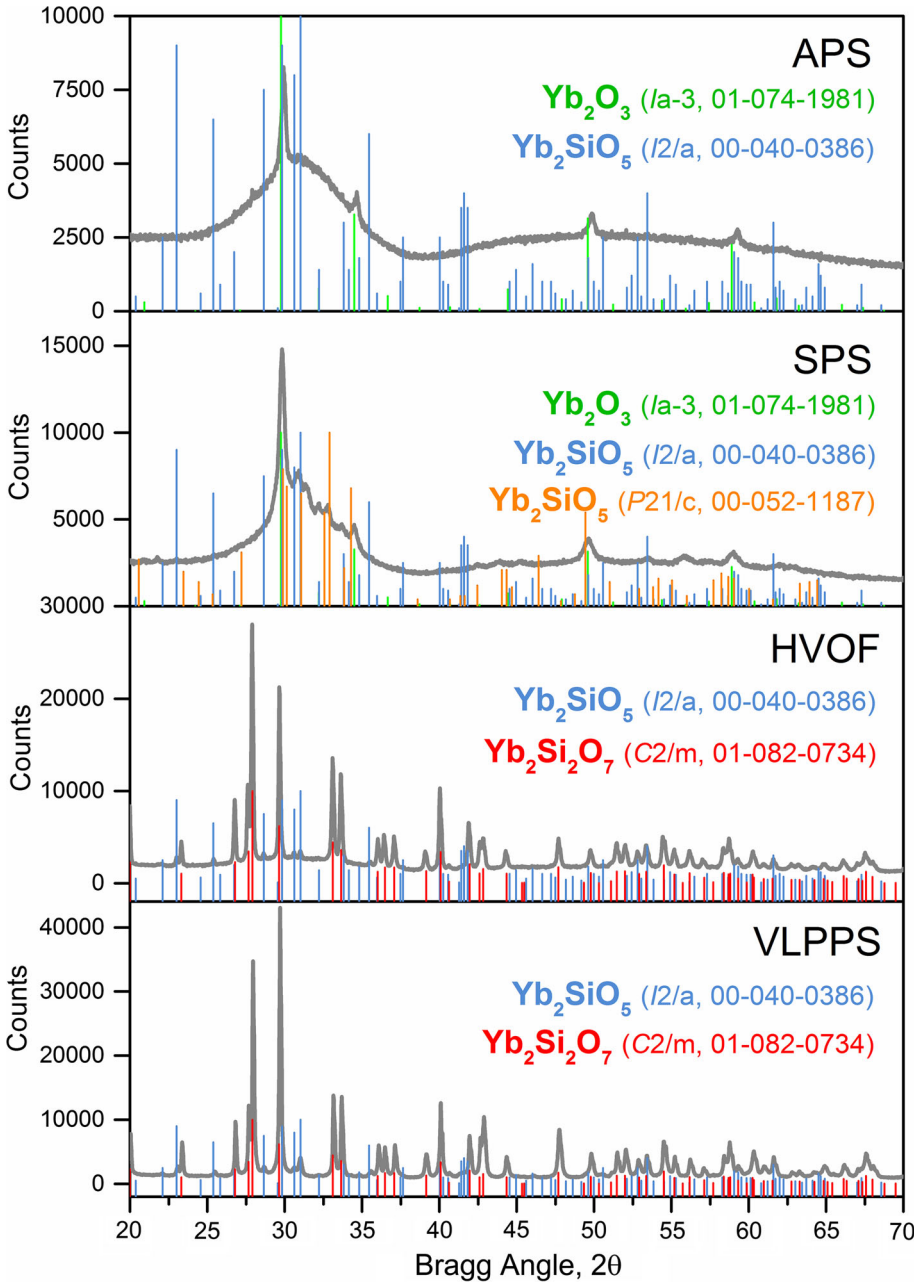

Fig. 4 XRD patterns of as-sprayed $Yb_2Si_2O_7$ coatings deposited by means of different thermal spray techniques

temperature quickly dropped down to 400-600 °C until the spraying began and was monitored to be in this range during the deposition. In the controlled atmosphere of the VLPPS chamber, the temperature drop was relatively minor ($\approx$50 K) and the deposition temperatures during plasma spraying were recorded to be 980 °C. Besides, while samples rapidly cooled to room temperature after APS and SPS depositions were completed, it was possible to retain high temperatures of the sample in the VLPPS chamber following deposition. To further reduce the cooling rate, the sample was heated by the plasma flame after the deposition likewise the previous substrate heating.

Table 4 Phase composition and amorphous content of the as-sprayed coatings determined by the PONKCS method

	APS	SPS	HVOF	VLPPS
$Yb_2Si_2O_7$, wt.%			49.0	93.0
Yb_2SiO_5 (I2/*a*), wt.%	0.5	2.0	3.0	5.0
Yb_2SiO_5 (P21/*c*), wt.%		2.5		
Yb_2O_3, wt.%	2.5	8.5		
Amorphous, wt.%	97.0	87.0	48.0	2.0
Deposition temperature, °C	575	500	125-150	980

Deposition temperatures recorded for each process are also given for a comparison

The plasma power used for the heating was gradually reduced within the given time, and the sample was steadily cooled to room temperature. As a result of this heat management in the VLPPS process, highly crystallized $Yb_2Si_2O_7$ as-sprayed coatings were obtained, as shown in Fig. 4, in contrast to APS and SPS methods. A quantitative comparison of the amorphous contents in each thermally sprayed coating can also be found in Table 4.

The crystallization of fully molten particles was found to be strongly reliant on deposition temperatures by comparing the results of plasma spraying processes with each other. While ~98% crystallinity was achieved in the VLPPS process thanks to high deposition temperature as well as the post-deposition plasma heating (effect of it on the crystallinity and microstructure will be further discussed below), very high amorphous contents (~97% in APS, ~87% in SPS) was obtained at moderate deposition temperatures. On the other hand, although the highest deposition temperature obtained with the HVOF flame was 150 °C, PONKCS analysis results suggest ~48% amorphous content in the HVOF coating, which is significantly lower than that of APS and SPS coatings. This higher crystallinity in the HVOF coating can be attributed to partially molten/non-molten particle deposition in this method (microstructure will be shown and discussed in the next section) which preserve the crystalline structure as shown in a different study (Ref 39).

Phase Composition

The reflection peaks in the patterns of the coatings (Fig. 4) can be indexed using the diffraction patterns of monoclinic $Yb_2Si_2O_7$ (*C*2/*m*, JCPDS No 01-082-0734), monoclinic Yb_2SiO_5 (*I*2/*a*, JCPDS No 00-040-0386), monoclinic Yb_2SiO_5 ($P2_1/c$, JCPDS No 00-052-1187), and cubic Yb_2O_3 (*Ia*-3, JCPDS No 01-074-1981). Accordingly, crystalline phases in the highly amorphous APS and SPS coatings were found to be Yb_2O_3 (*Ia*-3) and Yb_2SiO_5 (*I*2/*a*, $P2_1/c$). The Yb_2SiO_5 phase with the monoclinic symmetry of $P2_1/c$ was obtained as an intermediate oxidation product of $Yb_4Si_2O_7N_2$ and introduced as a metastable modification of Yb_2SiO_5 for the first time by Kolitsch et al. (Ref 40). More recently, Heng et al. and Richards et al. reported the formation of the Yb_2SiO_5 $P2_1/c$ phase in magnetron-sputtered Yb heavily doped silicon oxide coatings, and in the plasma sprayed $Yb_2Si_2O_7$ (and Yb_2SiO_5) coatings, respectively (Ref 26, 41). In both studies, the metastable Yb_2SiO_5 $P2_1/c$ phase was transformed to Yb_2SiO_5 *I*2/*a* after annealing at 1200 °C. Since the Yb_2O_3 phase was not detected in the feedstocks, its presence in the APS and SPS coatings can be explained by silicon loss during spraying, according to the Yb_2O_3-SiO_2 binary phase diagram (Ref 42) (Fig. 5). Silicon loss from the $Yb_2Si_2O_7$ interoxide compound leads to a shift in the composition toward the Yb-rich region. Depending on the extent of the loss, the Yb-rich composition either crystallizes partially or

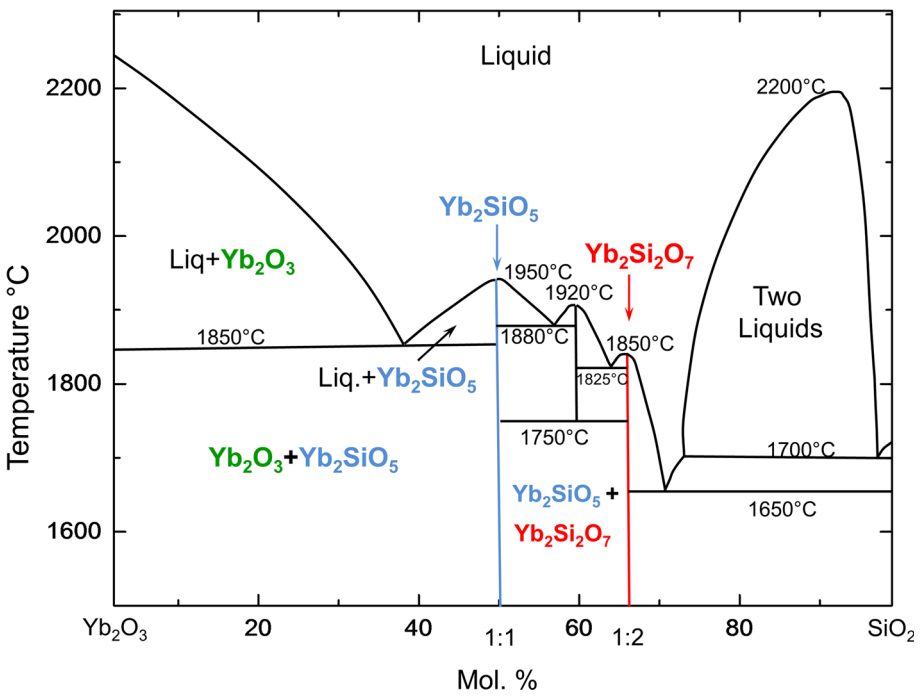

Fig. 5 Yb_2O_3-SiO_2 pseudo-binary phase diagram. Redrawn from Ref 37

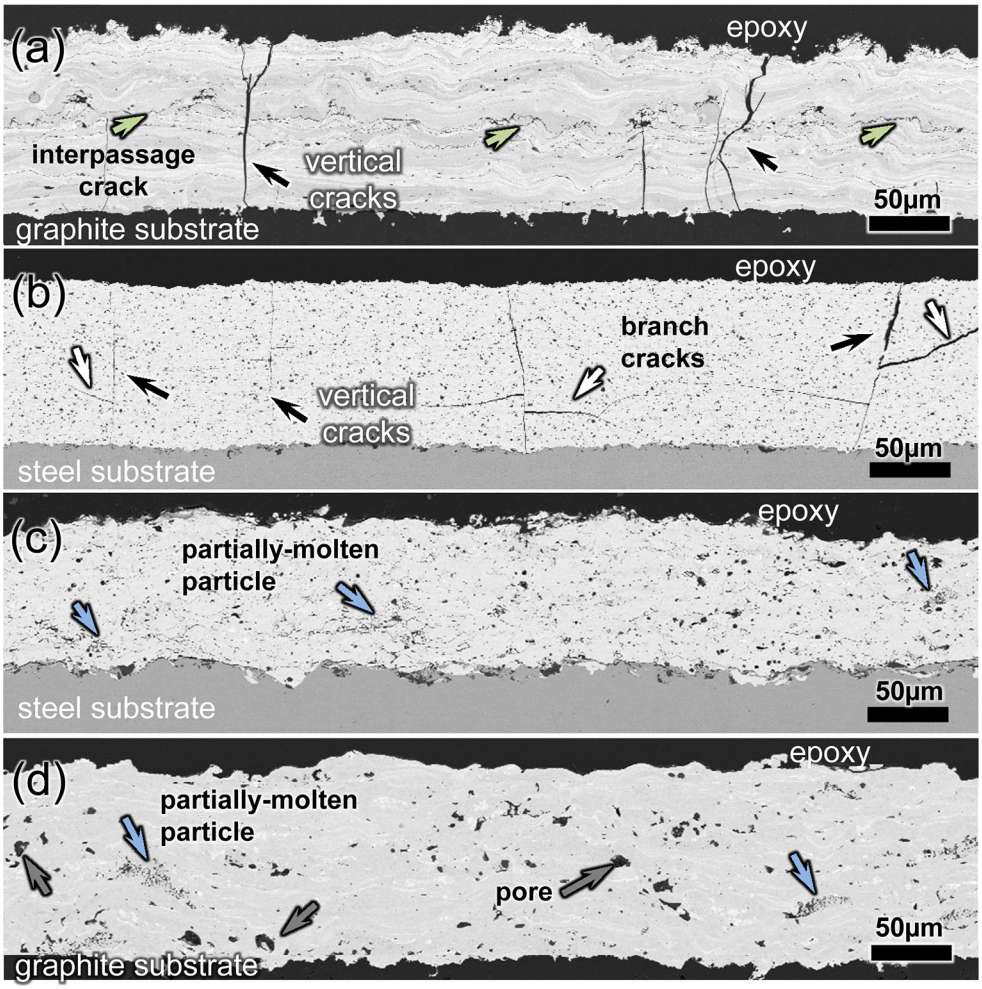

Fig. 6 Backscattered SEM (BSE-SEM) micrographs of as-sprayed $Yb_2Si_2O_7$ coatings by (a) APS, (b) SPS, (c) HVOF, and (d) VLPPS thermal spray methods. Black arrows indicate the vertical cracks, green arrows indicate the interpassage crack, white arrows indicate branch cracks, blue arrows indicate the partially or non-molten particles, and gray arrows indicate the pores in the images

completely into an equilibrium Yb_2SiO_5 phase or eutectic solidification occurs with an eventual Yb_2O_3 product. Depending on whether the composition falls into a hypereutectic or hypoeutectic region, a proeutectic Yb_2SiO_5 or Yb_2O_3 forms until the composition reaches the eutectic composition where the remaining solidification follows the eutectic reaction.

Microstructure

Figure 6 shows a comparison of the microstructures of $Yb_2Si_2O_7$ coatings deposited using the APS, HVOF, SPS, and VLPPS techniques. Due to the elevated substrate temperature by plasma torch prior to spraying and subsequent high-power spraying conditions, fully molten particle deposition with no intrasplat cracks is observed in the APS deposit. A small number of interlamellar cracks in the deposit also imply the remelting of deposited splats with the arrival of the next splats and the promoted diffusion between them at these high deposition temperatures. Nevertheless, a clear interface crack between the two spray passages of the APS deposit is visible (Fig. 6a). Furthermore, cracks penetrating vertically into the thickness of the coating are found to be present in the APS deposit with a crack density of 3 cracks/mm. Possibly, the origin of these cracks is CTE mismatch resulting in tensile stress development in the highly amorphous and dense coating during the cooling from high deposition temperature to room temperature.

A vertical crack network coupled with branch cracks was also observed in the SPS-deposited $Yb_2Si_2O_7$ coating on the steel substrate with evenly distributed very small pores (Fig. 6b). Considering that the steel substrate probably has higher CTE than the coating in this case, vertical

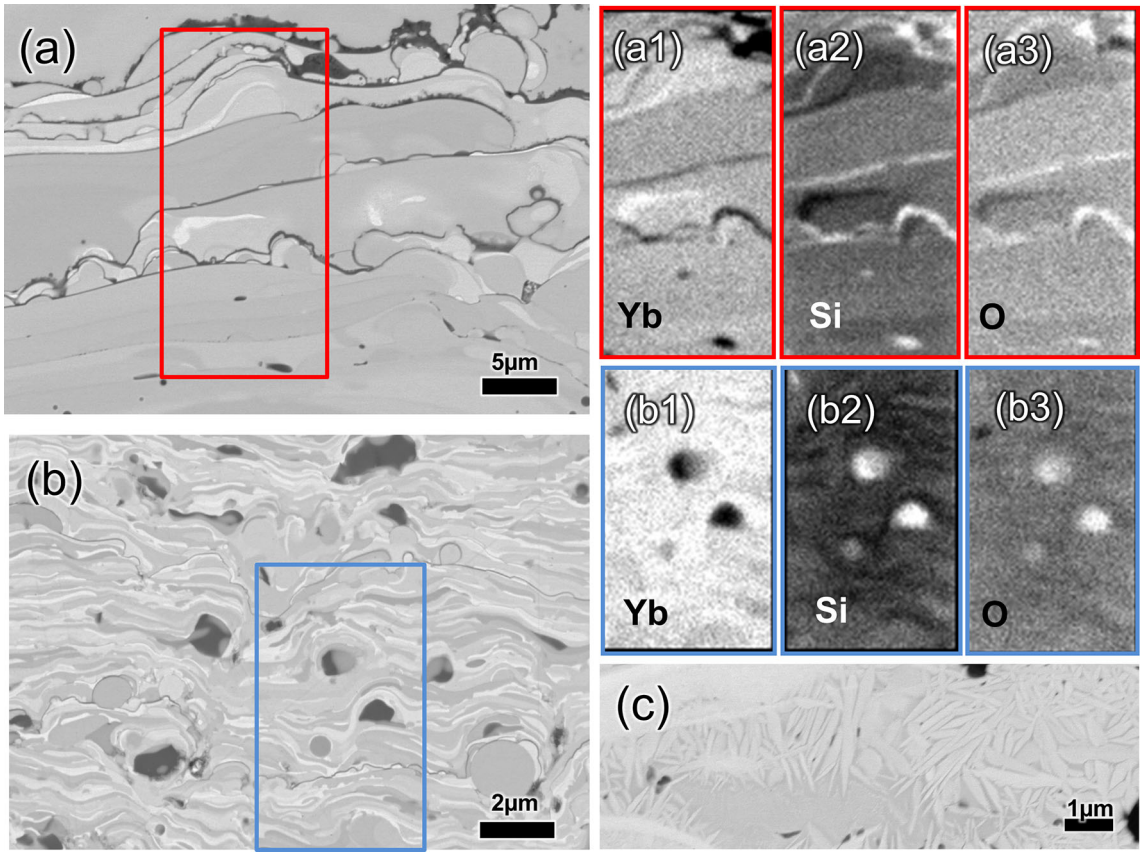

Fig. 7 High-magnification BSE-SEM micrographs of as-sprayed $Yb_2Si_2O_7$ coatings by (a) APS and (b) (SPS). Red and blue boxes indicate the recorded elemental mapping region of the images by EDS (a1-a3, b1-b3). Elongated crystal growth observed in the (c) APS-deposited $Yb_2Si_2O_7$ coating (Color figure online)

cracks found in the SPS coating can be called as segmentation cracks and attributed to stress relaxation in the coating during the deposition process. Segmentation crack formation in the SPS coating is a well-known phenomenon and typically associated with the high torch power used to evaporate the suspension liquid and short spray distances in this process (Ref 43, 44).

Figure 6(c) and (d) shows the cross section of HVOF and VLPPS $Yb_2Si_2O_7$ coatings with relatively dense and vertical crack-free microstructures. Splat/splat boundaries are difficult to discern in these deposits, indicating good adhesion between the splats over a large contact area. Nevertheless, some fine porosity and microcracks are present, resulting from non-molten or partially molten particles embedded in the HVOF microstructure. Some partially molten particles that bonded well with the melted part are also observed in the VLPPS coating. The porosity of HVOF and VLPPS coatings was determined to be 6.6 ± 0.8 and $3.6 \pm 0.4\%$, respectively, by image analysis.

Higher-magnification BSE-SEM images of the APS and SPS coatings with EDS elemental maps are given in Fig. 7(a) and (b). Between the changing material contrasts from white to dark gray, various intermediate gray shades appear in the cross section of the highly amorphous coatings. EDS maps reveal that Yb-rich regions are white due to the high average atomic number, while different gray shades from light to dark show the gradually increasing Si-containing mixtures. Moreover, a number of randomly oriented and elongated fine crystallites were observed in the amorphous matrix of the APS coating, as shown in Fig. 7(c). However, a reliable identification of the composition of these crystallites was not possible due to their small size.

Figure 8(a) and (b) shows the high-magnification BSE-SEM images of highly crystalline HVOF and VLPPS coatings. According to the XRD data, two phases (Yb_2SiO_5 and $Yb_2Si_2O_7$) are present in these coatings, although more than two different material contrasts were observed in the images. EDS analyses reveal a compositional difference between the white (Yb-rich) and gray (Yb-poor) regions, but not among the areas with various shades of gray. Furthermore, a number of very fine structures were observed in the VLPPS coating, in which one phase is embedded in the matrix of another phase(s) without any

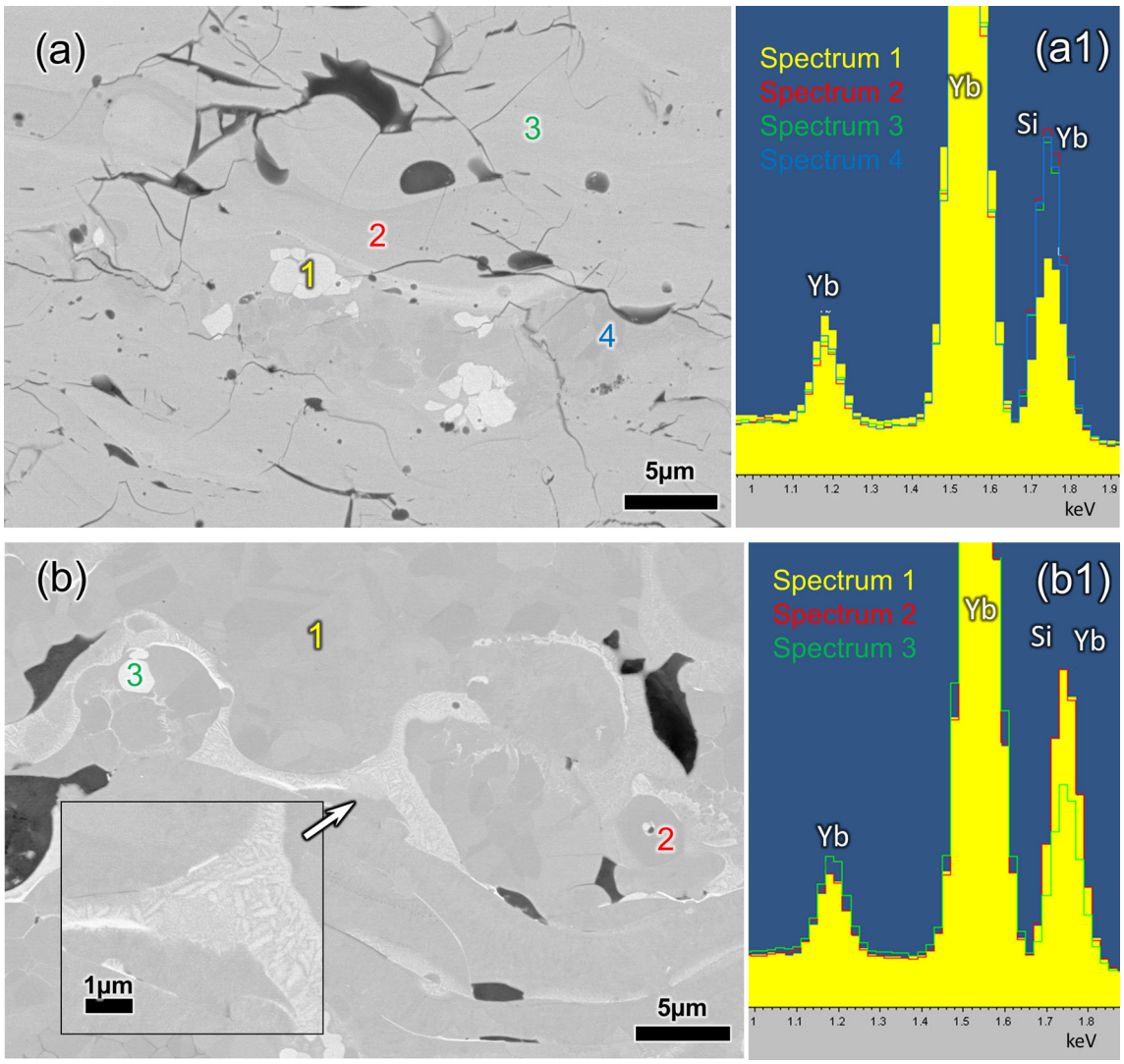

Fig. 8 High-magnification BSE-SEM micrographs of as-sprayed $Yb_2Si_2O_7$ coatings by (a) HVOF, (b) VLPPS, and corresponding EDS spectra (a1 and b1). Inset in (b) displays a higher-magnification image of a splat boundary

apparent orientation relationships (Fig. 8b, inset). In particular, such structures were commonly found at the splat boundaries of the VLPPS coating, where the Si evaporation is likely most pronounced. It is possible that these very fine structures are the product of a eutectic solidification or a hypoeutectic/hypereutectic solidification that could not be determined by SEM.

Crack-free microstructures of the HVOF and VLPPS coatings can be related to their deposition conditions, residual stress states, and crystallinity. Relatively higher porosity, hence a better strain tolerance, and lower magnitude of CTE mismatch stresses stemming from colder deposition conditions can be assisting the crack-free microstructure in the HVOF process. In the VLPPS, even though the coating is denser and the deposition temperature is rather high, moderate cooling rates (owing to post-deposition plasma heating with gradually reduced power) can be preventing the crack formation. In order to investigate the effect of higher amorphous content (as well as the condition of cooling in the case of VLPPS) on the microstructure of HVOF and VLPPS coatings, further experiments were conducted. To that end higher amount of methane (200 slpm) giving the stoichiometric fuel/oxygen ratio to obtain maximum flame temperature was used in the HVOF process and no post-deposition plasma heating was applied in the VLPPS. Figure 9(a) and (b) shows the microstructure of these coatings, and their XRD patterns are given in Fig. 9(c). According to PONKCS analysis results, ~45 and ~75% crystallinity was obtained in these HVOF- and VLPPS-deposited coatings, respectively. The porosity of the HVOF and VLPPS coatings was measured to be $3.7 \pm 0.8\%$ and $4.2 \pm 0.6\%$ via image analysis

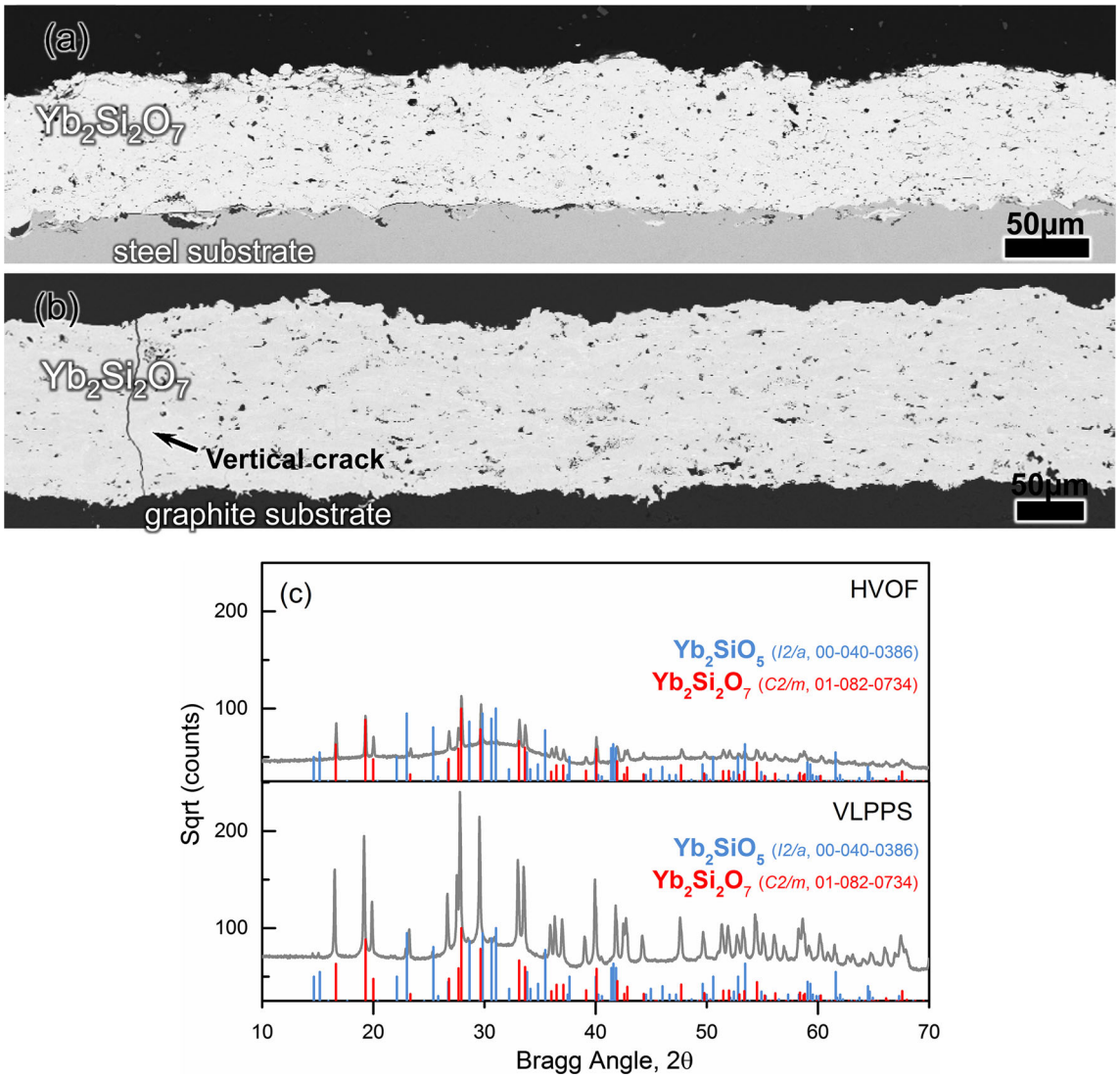

Fig. 9 SEM micrographs of (a) an HVOF coating deposited with stoichiometric methane/oxygen ratio (200/395) and (b) a VLPPS coating deposited without post-deposition plasma heating. The XRD patterns of these two coatings are given in (c)

(cracked regions were not evaluated in the analysis of VLPPS coating). The small reduction in the crystallinity and porosity of HVOF coating is clearly due to the better melting of the particles while higher amorphous content in the VLLPS coating implies that part of the crystallization takes place during the post-deposition plasma heating. Furthermore, it is evident from the presence of vertical cracks (6 cracks/cm) in VLPPS coating that increased cooling rate leads to development of higher magnitude of stresses in the as-sprayed coating. It is worth mentioning that change in the crystallinity is possibly affecting the mechanical properties of the coatings such as elastic modulus and fracture toughness, which may also play a role in the crack formation, but this remains unclear at this stage of the investigation.

Summary and Conclusions

$Yb_2Si_2O_7$ coatings were deposited by means of APS, HVOF, SPS, and VLPPS thermal spray methods using a commercial and an internally synthesized feedstock. The as-sprayed amorphous contents of the coatings were investigated and compared taking into consideration the deposition conditions (deposition temperature, holding time at high temperature) and particle melting states (molten or non-molten particle deposition) in different processes.

APS- and SPS-deposited coatings were found to be highly amorphous and vertically cracked. Moreover, evaporation of the Si-bearing species during deposition was found to be particularly pronounced in these processes,

leading to the formation of the Yb_2O_3 phase in the as-sprayed coatings.

Almost fully crystalline (~98%) and highly dense $Yb_2Si_2O_7$ coatings could be deposited in the VLPPS chamber as a result of the high deposition temperature and post-deposition plasma heating. It was also found that the latter is influential in preventing the vertical crack formation in the coating.

The HVOF process was found to yield relatively high crystalline (45-50%) coatings in contrast to APS- and SPS-deposited coatings (5-10%) due to the partially molten or non-molten particle deposition. The porosity content of HVOF coatings was found to be in the range of 4–7% depending on processing conditions. Despite having two times higher amorphous content than the VLPPS coatings (max. 50% vs. max. 25%) HVOF coatings revealed no vertical cracks. This implies that critically different residual stress states in these coatings due to thermal expansion mismatch and deposition temperatures are playing a major role in the crack formation, considering no significant differences in the porosity levels, chemistry as well as the thickness of the coatings.

It can be concluded that the VLPPS is the preferred method among others as an almost fully crystalline, dense coating microstructure without vertical cracks could be obtained with it. Nevertheless, it was found that the cooling conditions need to be carefully tuned to achieve such results. HVOF technique seems to be also promising, but further investigations are required to investigate the bonding of HVOF-sprayed particles on brittle silicon bond coat. Future studies will generally focus on adhesion of coatings as well as a better understanding of crack formation mechanisms for developing strategies to achieve the best performance. Furthermore, steam cycling tests are planned for validation of the coating systems.

References

1. E.J. Opila and R.E. Hann, Paralinear Oxidation of CVD SiC in Water Vapor, *J. Am. Ceram. Soc.*, 1997, **80**(1), p 197-205
2. R.C. Robinson and J.L. Smialek, SiC Recession Caused by SiO_2 Scale Volatility under Combustion Conditions: I, Experimental Results and Empirical Model, *J. Am. Ceram. Soc.*, 1999, **82**(7), p 1817-1825
3. E.J. Opila, J.L. Smialek, R.C. Robinson, D.S. Fox, and N.S. Jacobson, SiC Recession Caused by SiO_2 Scale Volatility under Combustion Conditions: II, Thermodynamics and Gaseous-Diffusion Model, *J. Am. Ceram. Soc.*, 1999, **82**(7), p 1826-1834
4. J.L. Smialek, R.C. Robinson, E.J. Opila, D.S. Fox, and N.S. Jacobson, SiC and Si_3N_4 Recession Due to SiO_2 Scale Volatility Under Combustor Conditions, *Adv. Compos. Mater.*, 1999, **8**(1), p 33-45
5. N.P. Bansal, Handbook of Ceramic Composites ed. by Narottam P. Bansal. [E-Book], Kluwer, 2005
6. N.S. Jacobson, Corrosion of Silicon-Based Ceramics in Combustion Environments, *J. Am. Ceram. Soc.*, 1993, **76**(1), p 3-28
7. K.N. Lee, Current Status of Environmental Barrier Coatings for Si-Based Ceramics, *Surf. Coat. Technol.*, 2000, **133-134**, p 1-7
8. H.E. Eaton, G.D. Linsey, K.L. More, J.B. Kimmel, J.R. Price, N. Miriyala, EBC Protection of SiC/SiC Composites in the Gas Turbine Combustion Environment, ASME Turbo Expo 2000: Power for Land, Sea, and Air, 2000, American Society of Mechanical Engineers, p V004T002A018
9. H.E. Eaton, G.D. Linsey, E.Y. Sun, K.L. More, J.B. Kimmel, J.R. Price, N. Miriyala, EBC Protection of SiC/SiC Composites in the Gas Turbine Combustion Environment: Continuing Evaluation and Refurbishment Considerations, ASME Turbo Expo 2001: Power for Land, Sea, and Air, 2001, American Society of Mechanical Engineers, p V004T002A010
10. K.N. Lee, D.S. Fox, J.I. Eldridge, D. Zhu, R.C. Robinson, N.P. Bansal, and R.A. Miller, Upper Temperature Limit of Environmental Barrier Coatings Based on Mullite and BSAS, *J. Am. Ceram. Soc.*, 2003, **86**(8), p 1299-1306
11. K.N. Lee, D.S. Fox, and N.P. Bansal, Rare Earth Silicate Environmental Barrier Coatings for SiC/SiC Composites and Si_3N_4 Ceramics, *J. Eur. Ceram. Soc.*, 2005, **25**(10), p 1705-1715
12. K.N. Lee, R.A. Miller, and N.S. Jacobson, New Generation of Plasma-Sprayed Mullite Coatings on Silicon Carbide, *J. Am. Ceram. Soc.*, 1995, **78**(3), p 705-710
13. C.M. Weyant and K.T. Faber, Processing–Microstructure Relationships for Plasma-Sprayed Yttrium Aluminum Garnet, *Surf. Coat. Technol.*, 2008, **202**(24), p 6081-6089
14. C. Friedrich, R. Gadow, and T. Schirmer, Lanthanum Hexaaluminate—A New Material for Atmospheric Plasma Spraying of Advanced Thermal Barrier Coatings, *J. Therm. Spray Technol.*, 2001, **10**(4), p 592-598
15. G. Pracht, R. Vaßen, and D. Stöver, Lanthanum-Lithium Hexaaluminate—A New Material for Thermal Barrier Coatings in Magnetoplumbite Structure—Material and Process Development. *Advanced Ceramic Coatings and Interfaces: Ceramic Engineering and Science Proceedings*, Wiley, 2008, p 87-99
16. K.N. Lee, R.A. Miller, and N.S. Jacobson, Plasma Sprayed Mullite Coatings on Silicon-Base Ceramics, ed., Google Patents, 1995
17. B.T. Richards and H.N.G. Wadley, Plasma Spray Deposition of Tri-Layer Environmental Barrier Coatings, *J. Eur. Ceram. Soc.*, 2014, **34**(12), p 3069-3083
18. F. Stolzenburg, P. Kenesei, J. Almer, K.N. Lee, M.T. Johnson, and K.T. Faber, The Influence of Calcium–Magnesium–Aluminosilicate Deposits on Internal Stresses in $Yb_2Si_2O_7$ Multilayer Environmental Barrier Coatings, *Acta Mater.*, 2016, **105**, p 189-198
19. H. Zhao, B.T. Richards, C.G. Levi, and H.N.G. Wadley, Molten Silicate Reactions with Plasma Sprayed Ytterbium Silicate Coatings, *Surf. Coat. Technol.*, 2016, **288**, p 151-162
20. B.T. Richards, K.A. Young, F. de Francqueville, S. Sehr, M.R. Begley, and H.N.G. Wadley, Response of Ytterbium Disilicate–Silicon Environmental Barrier Coatings to Thermal Cycling in Water Vapor, *Acta Mater.*, 2016, **106**, p 1-14
21. S. Ueno, T. Ohji, and H.-T. Lin, Recession Behavior of a Silicon Nitride with Multi-layered Environmental Barrier Coating System, *Ceram. Int.*, 2007, **33**(5), p 859-862
22. S. Ramasamy, S.N. Tewari, K.N. Lee, R.T. Bhatt, and D.S. Fox, Slurry Based Multilayer Environmental Barrier Coatings for Silicon Carbide and Silicon Nitride Ceramics—I. Processing, *Surf. Coat. Technol.*, 2010, **205**(2), p 258-265
23. M.P. Appleby, D. Zhu, and G.N. Morscher, Mechanical Properties and Real-Time Damage Evaluations of Environmental Barrier Coated SiC/SiC CMCs Subjected to Tensile Loading Under Thermal Gradients, *Surf. Coat. Technol.*, 2015, **284**, p 318-326

24. P. Mechnich, Y_2SiO_5 Coatings Fabricated by RF Magnetron Sputtering, *Surf. Coat. Technol.*, 2013, **237**, p 88-94
25. D.D. Jayaseelan, S. Ueno, T. Ohji, and S. Kanzaki, Sol–Gel Synthesis and Coating of Nanocrystalline $Lu_2Si_2O_7$ on Si_3N_4 Substrate, *Mater. Chem. Phys.*, 2004, **84**(1), p 192-195
26. B.T. Richards, H. Zhao, and H.N.G. Wadley, Structure, Composition, and Defect Control During Plasma Spray Deposition of Ytterbium Silicate Coatings, *J. Mater. Sci.*, 2015, **50**(24), p 7939-7957
27. B.T. Richards, S. Sehr, F. de Franqueville, M.R. Begley, and H.N.G. Wadley, Fracture Mechanisms of Ytterbium Monosilicate Environmental Barrier Coatings During Cyclic Thermal Exposure, *Acta Mater.*, 2016, **103**, p 448-460
28. G. Mauer, M.O. Jarligo, D.E. Mack, and R. Vaßen, Plasma-Sprayed Thermal Barrier Coatings: New Materials, Processing Issues, and Solutions, *J. Therm. Spray Technol.*, 2013, **22**(5), p 646-658
29. X.Q. Cao, R. Vassen, W. Jungen, S. Schwartz, F. Tietz, and D. Stöver, Thermal Stability of Lanthanum Zirconate Plasma-Sprayed Coating, *J. Am. Ceram. Soc.*, 2001, **84**(9), p 2086-2090
30. M.O. Jarligo, D.E. Mack, R. Vassen, and D. Stöver, Application of Plasma-Sprayed Complex Perovskites as Thermal Barrier Coatings, *J. Therm. Spray Technol.*, 2009, **18**(2), p 187-193
31. M.O. Jarligo, G. Mauer, D. Sebold, D.E. Mack, R. Vaßen, and D. Stöver, Decomposition of $Ba(Mg_{1/3}Ta_{2/3})O_3$ Perovskite During Atmospheric Plasma Spraying, *Surf. Coat. Technol.*, 2012, **206**(8-9), p 2515-2520
32. K. Korpiola, J.P. Hirvonen, L. Laas, and F. Rossi, The Influence of Nozzle Design on HVOF Exit Gas Velocity and Coating Microstructure, *J. Therm. Spray Technol.*, 1997, **6**(4), p 469-474
33. N. Schlegel, S. Ebert, G. Mauer, and R. Vaßen, Columnar-Structured Mg-Al-Spinel Thermal Barrier Coatings (TBCs) by Suspension Plasma Spraying (SPS), *J. Therm. Spray Technol.*, 2015, **24**(1), p 144-151
34. A. Vardelle, C. Moreau, J. Akedo, H. Ashrafizadeh, C.C. Berndt, J.O. Berghaus, M. Boulos, J. Brogan, A.C. Bourtsalas, A. Dolatabadi, M. Dorfman, T.J. Eden, P. Fauchais, G. Fisher, F. Gaertner, M. Gindrat, R. Henne, M. Hyland, E. Irissou, E.H. Jordan, K.A. Khor, A. Killinger, Y.-C. Lau, C.-J. Li, L. Li, J. Longtin, N. Markocsan, P.J. Masset, J. Matejicek, G. Mauer, A. McDonald, J. Mostaghimi, S. Sampath, G. Schiller, K. Shinoda, M.F. Smith, A.A. Syed, N.J. Themelis, F.-L. Toma, J.P. Trelles, R. Vassen, and P. Vuoristo, The 2016 Thermal Spray Roadmap, *J. Therm. Spray Technol.*, 2016, **25**(8), p 1376-1440
35. N.V.Y. Scarlett and I.C. Madsen, Quantification of Phases with Partial or No Known Crystal Structures, *Powder Diffr.*, 2006, **21**(4), p 278-284
36. J.B. Nelson and D.P. Riley, The Thermal Expansion of Graphite from 15 °C to 800 °C: Part I. Experimental, *Proceedings of the Physical Society*, 1945, **57**(6), p 477
37. J. Felsche, *The Crystal Chemistry of the Rare-Earth Silicates*, Rare Earths ed., Springer, Berlin, 1973, p 99-197
38. D. Hülsenberg, A. Harnisch, and A. Bismarck, *Microstructuring of Glasses*, Springer, Berlin, 2008
39. E. Bakan, G. Mauer, Y. Sohn, D. Koch, and R. Vaßen, Application of High-Velocity Oxygen-Fuel (HVOF) Spraying to the Fabrication of Yb-Silicate Environmental Barrier Coatings, *Coatings*, 2017, **7**(4), p 55
40. U. Kolitsch, V. Ijevskii, H.J. Seifert, I. Wiedmann, and F. Aldinger, Formation and General Characterization of a Previously Unknown Ytterbium Silicate (A-Type Yb_2SiO_5), *J. Mater. Sci.*, 1997, **32**(23), p 6135-6139
41. C.L. Heng, J.T. Li, W.Y. Su, Z. Han, P.G. Yin, and T.G. Finstad, The Formation of Yb Silicates and Its Luminescence in Yb Heavily Doped Silicon Oxides After High Temperature Annealing, *Opt. Mater.*, 2015, **42**, p 17-23
42. N.A. Toropov and I.A. Bondar', Silicates of the Rare Earth Elements, *Bull. Acad. Sci. USSR Div. Chem. Sci.*, 1961, **10**(8), p 1278-1285
43. R. Vaßen, H. Kaßner, G. Mauer, and D. Stöver, Suspension Plasma Spraying: Process Characteristics and Applications, *J. Therm. Spray Technol.*, 2010, **19**(1), p 219-225
44. D. Waldbillig and O. Kesler, Effect of Suspension Plasma Spraying Process Parameters on YSZ Coating Microstructure and Permeability, *Surf. Coat. Technol.*, 2011, **205**(23-24), p 5483-5492